

Scalable Programming of LaAlO₃/SrTiO₃ Interfaces via Ultra-Low-Voltage Electron-Beam Lithography

Dengyu Yang, Ranjani Ramachandran, Muqing Yu, Kitae Eom, Kyoungjun Lee, Patrick Irvin, Chang-Beom Eom, and Jeremy Levy*

Interface engineering at complex oxide heterostructures enables a wide range of electronic functionalities critical for next-generation devices. Here it is demonstrated that ultra-low-voltage electron beam lithography (ULV-EBL) creates high-quality mesoscale structures at LaAlO₃/SrTiO₃ (LAO/STO) interfaces with greater efficiency than conventional methods. Nanowires, tunnel barriers, and electron waveguides are successfully patterned that exhibit distinctive transport characteristics including 1D superconductivity, nonlinear current–voltage behavior, and ballistic electron flow. While conductive atomic force microscopy (c-AFM) previously enabled similar interface modifications, ULV-EBL provides significantly faster patterning speeds (10 mm s⁻¹ vs 1 μm s⁻¹), wafer-scale capability (>(10 cm)² vs <(90 μm)²), and maintenance of pattern quality under vacuum conditions. Additionally, an efficient oxygen plasma treatment method is developed for pattern erasure and surface cleaning, which reveals novel surface reaction dynamics at oxide interfaces. These capabilities establish ULV-EBL as a versatile approach for scalable interface engineering in complex oxide heterostructures, with potential applications in reconfigurable electronics, sensors, and oxide-based devices.

its remarkable properties, including tunable metal-insulator transitions,^[3] superconductivity,^[4,5] ferromagnetism,^[6] and strong spin-orbit coupling,^[7,8] all co-existing within a single material system. These functionalities arise from the complex interplay of electronic correlations, lattice distortions, and interfacial effects that can be locally controlled through external stimuli, making LAO/STO an ideal platform for interface engineering.

Local modification of the LAO/STO interface has been predominantly achieved through conductive atomic force microscope (c-AFM) lithography,^[9,10] a technique that enables reversible nanoscale control of the metal-insulator transition. By applying an appropriate bias voltage to an AFM tip scanned across the LAO surface, the interfacial conductivity can be locally switched between insulating and conducting states with nanometer precision. This

approach has enabled the creation of reconfigurable nanoelectronic devices^[10–14] and revealed fundamental insights into the nature of superconductivity at the LAO/STO interface, such as its intrinsic 1D character^[15] and the existence of exotic electron pairing states.^[16,17]

Despite these achievements, c-AFM lithography faces significant limitations that hinder its practical application for large-scale interface engineering. The technique is inherently slow, with typical writing speeds of approximately 1 μm s⁻¹, and confined to relatively small areas dictated by the scan range of commercial AFMs (typically < 90 μm × 90 μm). Moreover, devices created using c-AFM lithography often exhibit volatility, with patterns spontaneously erasing over hour-long timescales in ambient conditions, which constrains the complexity and stability of nanostructures that can be reliably fabricated.

To overcome these limitations, we have developed ultra-low-voltage electron beam lithography (ULV-EBL) as an alternative approach for programming the LAO/STO interface.^[18] This technique employs a low-energy electron beam (100–1000 eV) to induce similar conductivity changes as c-AFM but offers significantly faster patterning speeds (10 mm s⁻¹ vs 1 μm s⁻¹) and larger working areas (> (10 cm)² vs < (90 μm)²). While c-AFM can reach a resolution of 2 nm,^[10] ULV-EBL achieves 10 nm resolution^[18] with the added advantage of operation under vacuum conditions, which inhibits device degradation that commonly occurs with

1. Introduction

Complex oxide interfaces, particularly those between LaAlO₃ (LAO) and SrTiO₃ (STO), represent one of the most versatile materials platforms for exploring emergent electronic phenomena.^[1] The discovery of a 2D electron gas (2DEG) at the LAO/STO interface^[2] has sparked extensive research into

D. Yang, R. Ramachandran, M. Yu, P. Irvin, J. Levy
Department of Physics and Astronomy
University of Pittsburgh
Pittsburgh, PA 15260, USA
E-mail: jlevy@pitt.edu

K. Eom, K. Lee, C.-B. Eom
Department of Materials Science and Engineering
University of Wisconsin-Madison
Madison, WI 53706, USA

 The ORCID identification number(s) for the author(s) of this article can be found under <https://doi.org/10.1002/admi.202500442>

© 2025 The Author(s). Advanced Materials Interfaces published by Wiley-VCH GmbH. This is an open access article under the terms of the [Creative Commons Attribution](https://creativecommons.org/licenses/by/4.0/) License, which permits use, distribution and reproduction in any medium, provided the original work is properly cited.

DOI: 10.1002/admi.202500442

Table 1. Comparison between c-AFM and ULV-EBL techniques.

	c-AFM	ULV-EBL
Platform	AFM	SEM
Environment	atmosphere	<10 ⁻⁶ mbar vacuum
"Pen"	AFM tip	electron beam
Scale size	<(90 μm) ²	>(10 cm) ²
Writing speed	1 μm s ⁻¹	10 mm s ⁻¹
in-situ erasing	negatively biased tip	oxygen plasma
Resolution	2 nm (Ref. [10])	10 nm (Ref. [18])

c-AFM's atmospheric patterning (Table 1). Furthermore, ULV-EBL can program the LAO/STO interface underneath van der Waals (vdW) overlayers,^[18–20] expanding the possibilities for creating hybrid material systems with engineered properties.

In this work, we extend the capabilities of ULV-EBL by demonstrating the creation of fundamental mesoscopic building blocks at the LAO/STO interface, including nanowires, tunnel barriers, and electron waveguides. We investigate their electronic transport properties, with a particular focus on the 1D superconductivity and ballistic transport characteristics. Additionally, we explore the use of oxygen plasma treatment as an efficient method for pattern erasure and surface cleaning, providing insights into the complex surface reaction mechanisms that govern the LAO/STO interface conductivity. These capabilities establish ULV-EBL as a versatile approach for scalable interface engineering in complex oxide heterostructures, enabling the development of advanced oxide-based electronic devices and providing a platform for exploring emergent phenomena at oxide interfaces.

2. Results

Complex-oxide heterostructures consisting of 3.4 unit cells of LAO were grown on TiO₂-terminated STO substrate using pulsed laser deposition (PLD) (See Experimental Section for details). The thickness of the LAO layer was precisely controlled by *in-situ* monitoring of oscillations from reflection high-energy electron diffraction (RHEED). Ti/Au electrodes were used to contact the interface, providing electrical connections to the 2D electron gas (2DEG) (see Experimental Section for more information). Initially, the interface was insulating, with a resistance greater than 5 GΩ.

2.1. On-Demand Nanoelectronic Devices

Here, we demonstrate the creation of several categories of nanoscale devices using ULV-EBL. These include nanowires, tunnel barriers, gates, and electron waveguides, device components that serve as building blocks for large-scale and complex nanoelectronic systems.

2.1.1. Nanowire and Conducting Channel

Nanowire devices at the LAO/STO interface exhibit interesting physics, such as ballistic transport,^[8,13,17] anomalous magnetic

states^[21] and 1D superconductivity,^[15] which are challenging to achieve in similar systems. A particularly notable finding, reported in Ref. [15], is that the superconducting critical current in c-AFM-patterned nanowires remains largely independent of channel width, indicating that superconductivity is confined to narrow edge regions rather than distributed across the full width.

In our previous work,^[18] we have demonstrated that ULV-EBL can be used to locally convert the LAO/STO interface from insulating to conducting, allowing the fabrication of nanostructures with sub-10 nm resolution. This method operates under vacuum and offers significantly faster patterning speed compared to c-AFM. We also showed that ULV-EBL-patterned nanowires can become superconducting below 300 mK, similar to those produced by c-AFM. Here, we investigate whether nanowires fabricated using ULV-EBL exhibit a similar 1D nature of superconductivity property. To explore this, ULV-EBL is used to create a series of conducting channels with different widths w .

As shown in Figure 1, three channels with different widths ($w_1 = 1 \mu\text{m}$, $w_2 = 200 \text{ nm}$, and $w_3 = 20 \text{ nm}$) are exposed using ULV-EBL in a pre-defined "canvas" region (Figure 1a,b), each with a length of $L = 10 \mu\text{m}$. Taking advantages of electrical feedthroughs to the e-beam chamber, we can have room temperature *in situ* electrical measurements during the ULV-EBL exposure. We observe a clear rise in conductance due to the e-beam exposure when the designed nanowires connect the metal electrodes, with conductance scaling proportional to the channel width (Figure 1c,d).

Transport measurements are performed at $T = 50 \text{ mK}$ using a dilution refrigerator. After ULV-EBL exposure and venting the SEM vacuum chamber using nitrogen, it takes less than 5 min to transfer the sample to the fridge, load the sample and start pumping. Upon cooling, the channels exhibit a transition from normal to superconducting behavior starting at $T = 350 \text{ mK}$. For instance, the 4-terminal resistance of the w_1 channel segment (Figure 2a) shows superconducting behavior with a residue resistance of $\approx 25 \Omega$. In a bulk superconductor, one would expect zero resistance in the superconducting state. However, in a quasi-1D geometry such as these patterned channels, phase-slip processes and associated fluctuations can suppress true long-range order, producing a finite residual resistance even in the superconducting regime^[22–24] The relatively small value of 25Ω suggests that such fluctuations are modest in our devices and that the patterned 2DEG retains high electronic quality. While there are very interesting thermal hysteresis effects reported,^[25] we did not track the conductivity hysteresis since the temperature measurements are not reliable during rapid temperature change.

Theoretically, for a 2D superconductor, the critical current is expected to scale linearly with the channel width, since a wider channel can support more parallel superconducting paths. However, in our experiments, the superconducting critical currents remain in the range of 15–20 nA regardless of the channel width (Figure 2b–e). This lack of scaling indicates a departure from conventional 2D behavior and suggests that superconductivity is not uniformly distributed across the channel. This phenomenon was first reported by Pai et al.^[15] in c-AFM-patterned LAO/STO devices, where it was described as evidence for the 1D nature of superconductivity at the interface. In this scenario, superconductivity is localized to narrow regions near the channel edges rather than spanning the entire width. This edge-confined behavior can

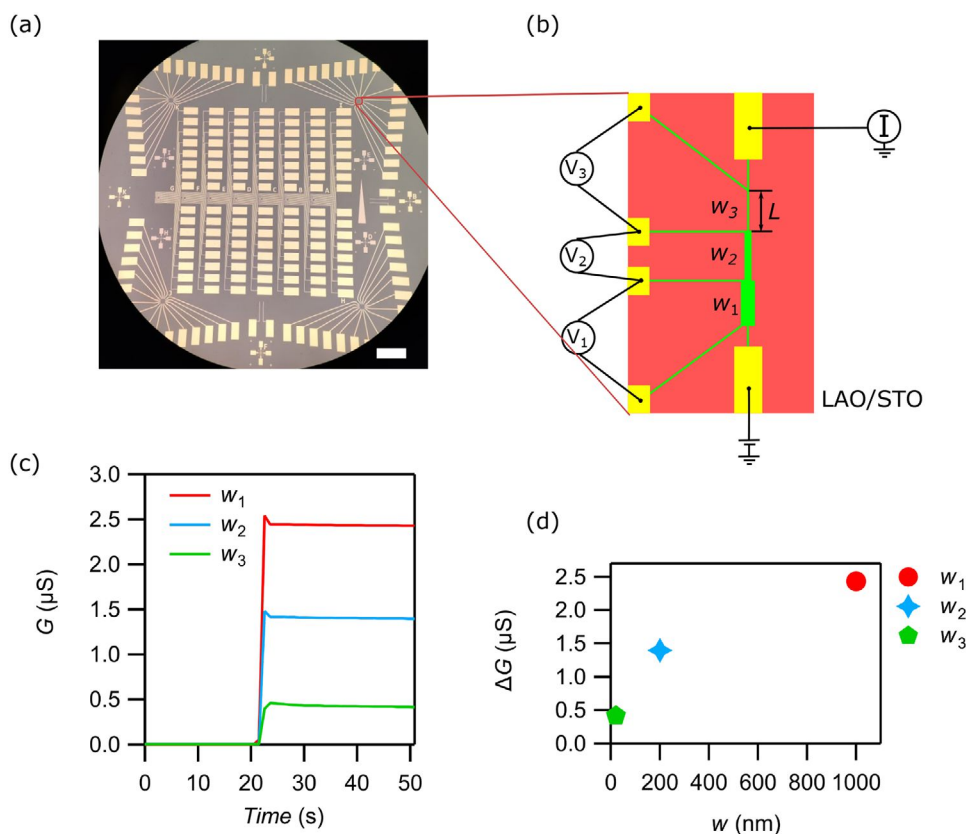


Figure 1. Patterned ULV-EBL conducting channels at LAO/STO. a) Optical image of the prepatterned electrodes. Red square denotes the defined canvas region. Scale bar shows 200 μm . b) Schematic diagram of a series of wires with different widths using ULV-EBL. The solid red part is the LAO/STO insulating sample. The solid yellow regions are the interface electrodes. Green lines denote conducting wires exposed by ULV-EBL. There is a 4-terminal transport characterization carried out at 50 mK. c) Conductance jump from ULV-EBL wiring of the three segments with different widths $w_1 = 1 \mu\text{m}$, $w_2 = 200 \text{ nm}$, and $w_3 = 20 \text{ nm}$. d) Conductance change with respect to the channel widths.

be understood in terms of the superconducting dome observed in STO and LAO/STO as a function of carrier concentration: superconductivity only emerges within an optimal doping window, while too many or too few carriers suppress it. Patterning the interface often leads to a carrier density gradient across the channel width, higher in the center and lower near the edges. As a result, only the edges may fall within the optimal doping range that supports superconductivity. Small variations are likely due to differences in local electrostatic environment or device geometry, as the superconducting region is confined to an optimally doped edge whose exact width is not directly measurable. Our results are consistent with this interpretation that this 1D superconducting behavior at the edges of wide channels, confirmed using the ULV-EBL technique. The observed independence of the critical current from channel width strongly supports the idea that superconductivity is confined to edge regions defined by the local doping environment.

2.1.2. Tunnel Barrier

A basic yet essential nanodevice is a 0D tunnel barrier, crucial for creating nanoelectronics and nanocircuits. Tunnel barriers act as potential energy obstacles that electrons must overcome, en-

abling manipulation of electron transport properties within nanodevices. This control is essential for achieving quantum confinement, regulating electron tunneling, and realizing complex device functions. Using c-AFM to create a barrier typically involves applying a negative bias voltage to the AFM tip along the nanowire, effectively cutting it (Figure 3a,b). Because ULV-EBL cannot erase features in situ, a barrier is created instead by leaving an unexposed gap of a chosen length while patterning the nanowire (Figure 3c).

To characterize the barrier, we examined its nonlinear current–voltage (I – V) response. A four-terminal transport measurement is set up in the ULV-EBL chamber under vacuum at room temperature (Figure 3d). Meanwhile, the gap distance d has been varied from 0 to 300 nm. The resulting I – V curves (Figure 3e) display nonlinear behavior with reduced current at low bias. The corresponding differential resistance dV/dI is shown in Figure 3f which features a high-resistance region. Barrier behavior was evident even when the gap was as small as 25 nm, demonstrating both the effectiveness of creating a barrier at the LAO/STO interface and the high resolution achievable with ULV-EBL.

Compared with previously reported barrier-type devices at the LAO/STO interface fabricated using c-AFM,^[10] ULV-EBL devices exhibit similar non-linear current–voltage characteristics, in

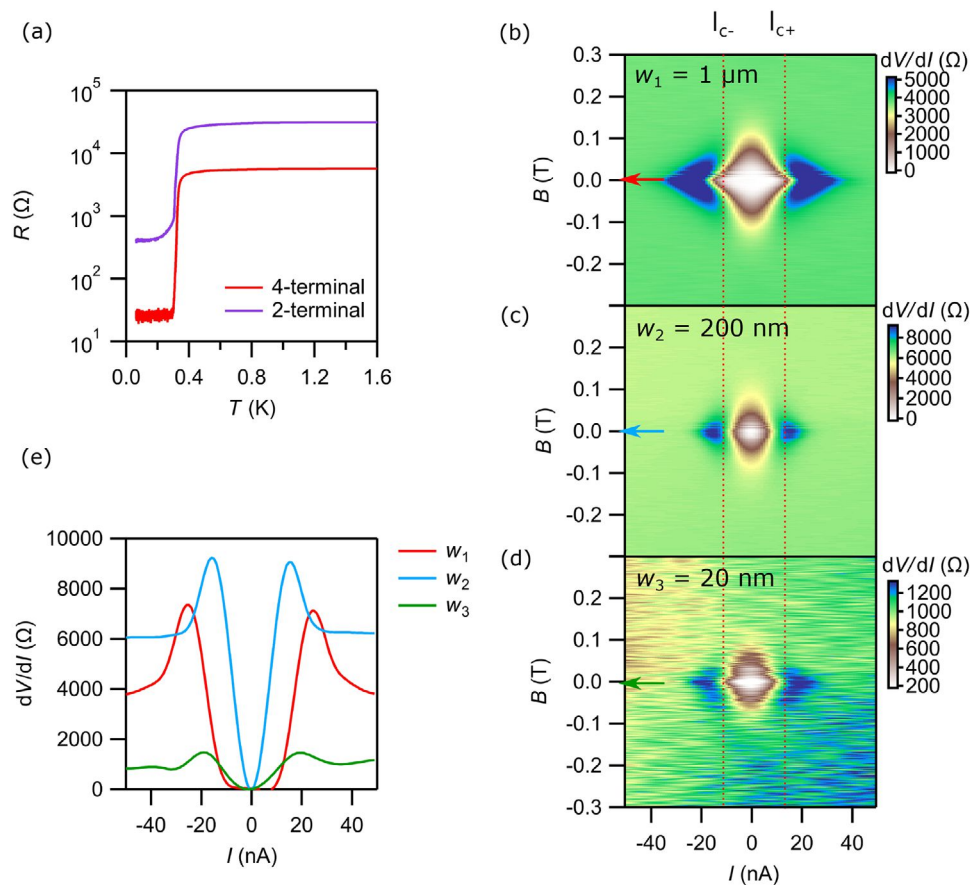


Figure 2. 1D nature of superconductivity. a) Resistance with respect to the temperature T during the cooldown process of the wire segment with width $w_1 = 1 \mu\text{m}$. Both 4-terminal and 2-terminal are shown here. b–d) Resistance dV/dI under magnetic field B . The red dotted lines denote the upper and lower critical currents ($I_{c\pm}$), which are similar for all three devices under different widths. The arrows show the linecuts at zero field in (e). e) Resistance dV/dI with respect to the four-terminal voltage V for tunnel barriers with different wire widths.

contrast to the linear IV response observed in nanowires. Photocurrent response in c-AFM-generated barrier-like junctions has been investigated previously,^[26] but has not yet been explored in devices patterned using ULV-EBL. The distinction lies in the patterning strategy and control parameters. In c-AFM, a barrier is created by cutting with a negative bias or applying a negative voltage pulse (Figure 3a,b), with the resulting properties determined indirectly by parameters such as the number of cuts, bias voltage, and cutting speed. The barrier dimensions in this case emerge from these conditions rather than being explicitly defined. In ULV-EBL, by contrast, the barrier gap is set directly by the lithographic layout, allowing precise and reproducible control over its size.

2.1.3. Electron Waveguide

One of the most important on-demand nanoelectronic devices is an electron waveguide. Quantized ballistic transport behavior is observed in LAO/STO waveguide devices, with a mean-free path $l_{MF} \sim 20 \mu\text{m}$.^[13] Adjusting the chemical potential by applying a sidegate voltage (V_{sg}) allows more electron subbands to contribute to the conductance, resulting in quantized conduc-

tance plateaus corresponding to the transport of electrons, electron pairs, and bound states of $n > 2$ electrons.^[17]

To create such waveguide devices using ULV-EBL, we combine the techniques described in the previous sections. We pattern a nanowire while leaving two gaps to serve as tunnel barriers, as described above. Figure 4a illustrates a nanowire segment with length $L = 500 \text{ nm}$ isolated from the source and drain by two tunnel barriers. The barriers here are made by leaving two 30 nm gaps while exposing the nanowire. We measure the conductance $G = dI/dV$ versus V_{sg} under zero-bias conditions and with out-of-plane magnetic field up to $B = \pm 18 \text{ T}$. The device exhibits clear conductance plateaus due to Landauer quantization,^[27,28] confirming the 1D ballistic nature of these devices. The magnetic-field dependent subband minima are revealed by plotting the transconductance dG/dV_{sg} . The first subband splits into two near $B = 3 \text{ T}$, which is well above the upper critical field of LAO/STO, consistent with previous reports of electron pairing without superconductivity.^[16]

In comparison with c-AFM patterned waveguide and nanowire devices,^[13] ULV-EBL devices exhibit similar underlying physics, including well-resolved subband features arising from ballistic transport and the phenomenon of electron pairing without superconductivity. Previous studies have demonstrated modulated

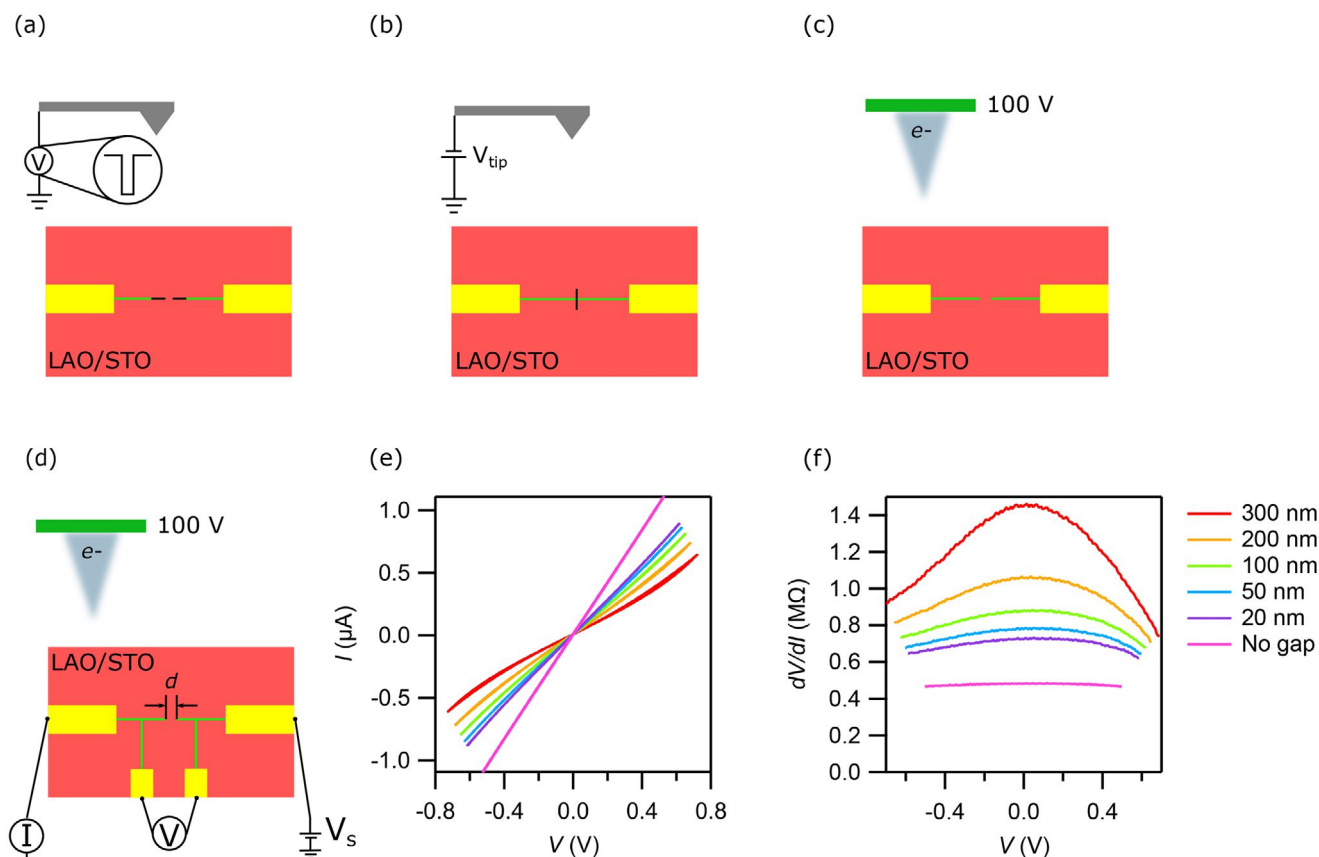


Figure 3. Barriers at LAO/STO interface. a) Schematic diagram of the creation of a barrier using the pulsed c-AFM tip. b) Schematic diagram of the creation of a barrier using a negatively biased c-AFM tip. c) Schematic diagram of creating a barrier using ULV-EBL. The red solid region shows the insulating LAO/STO sample. The green line is the nanowire. The solid orange region shows the interface electrodes. The black line shows the c-AFM tip trajectory. d) Schematic diagram of creating a barrier using ULV-EBL with transport measurement. The solid red part is the LAO/STO insulating sample. Solid yellow regions are the interface electrodes. Green lines denote conducting nanowires. There is a 4-terminal transport characterization carried out at room temperature under vacuum. e) Characterization of the I - V curve for tunnel barriers with different gap distances d . f) Resistance dV/dI with respect to the 4-terminal voltage V for tunnel barriers with different gap distances d .

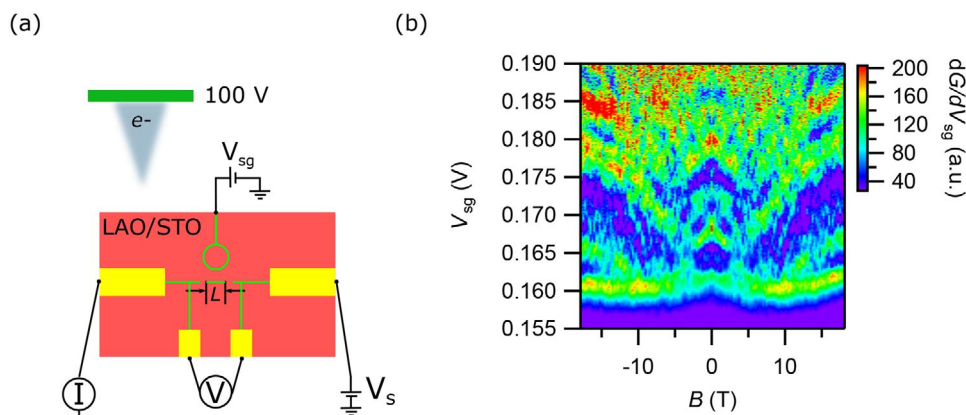


Figure 4. ULV-EBL waveguides on LAO/STO. a) Schematic diagram of a waveguide with main channel length L using ULV-EBL. The solid red part is the LAO/STO insulating sample. Solid yellow regions are the interface electrodes. Green lines denote conducting wires exposed by ULV-EBL. There is a 4-terminal transport characterization carried out at 50 mK. b) Transconductance dG/dV_{sg} with respect to the field B and V_{sg} .

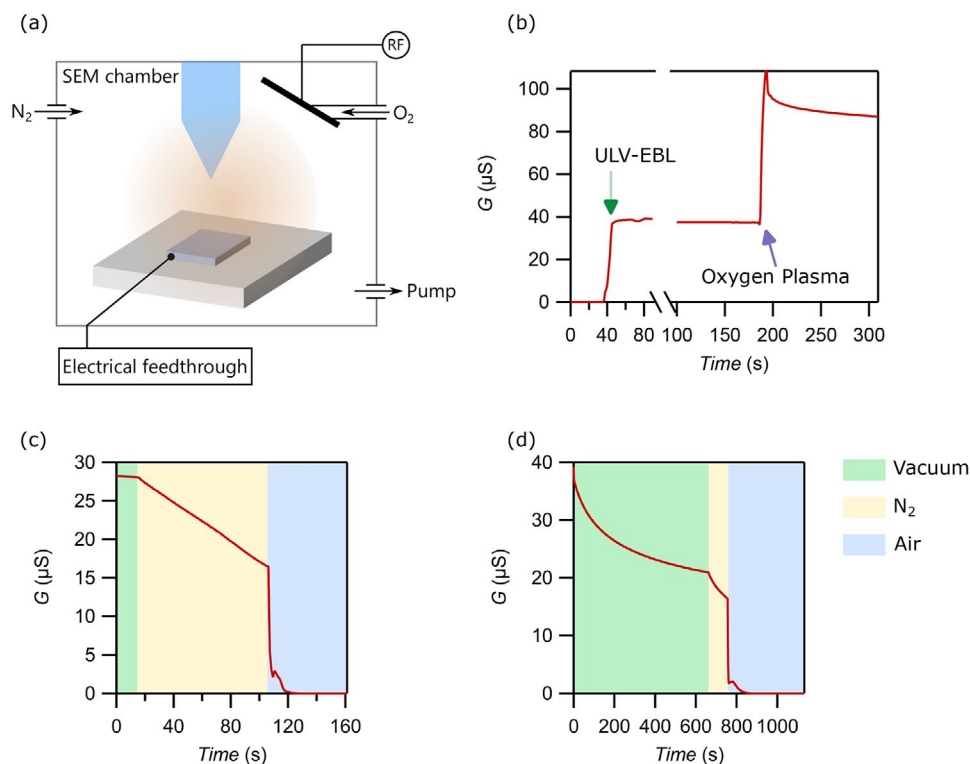


Figure 5. Erasing using oxygen plasma. a) Schematic diagram of the SEM chamber with oxygen plasma and in-situ electrical feedthrough. b) Monitoring the conductance G during ULV-EBL patterning (green arrow) and oxygen plasma treatment (purple arrow) in the EBL chamber. Oxygen plasma is 35 W for 6 seconds. c,d) Monitoring the conductance G after erasing by oxygen plasma in the EBL chamber. The green region is under chamber vacuum $\sim 10^{-6}$ mbar. The yellow region is when venting the chamber using nitrogen gas. The blue region is when the sample is exposed to the air. Panel (c) shows a shorter wait time in vacuum compared with (d).

waveguide devices at the LAO/STO interface, including 1D Kronig Penney type superlattices^[14] and serpentine waveguides,^[29] realized either through applied voltage modulation or deliberate real-space pattern design. Although such modulation has not yet been investigated with ULV-EBL, the ability to vary both the exposure dose and the pattern geometry offers an additional degree of freedom for engineering 1D nanowire devices in this direction. Moreover, the inherently fast writing speed and scalability of ULV-EBL open the possibility of extending superlattice engineering beyond one dimension, enabling systematic patterning of 2D superlattices.^[30] C-AFM devices generally display slightly higher quality, with reduced scattering in the transconductance spectrum, likely benefiting from their superior capability for precise local device definition. ULV-EBL, however, offers rapid patterning and scalability, enabling the fabrication of ballistic nanowires and waveguides while providing a practical route toward more complex device geometries.

2.2. Erasing LAO/STO Canvas with Oxygen Plasma Exposure

Unlike c-AFM, ULV-EBL lacks the capability to erase conducting patterns locally in situ. This creates an asymmetry in the write/erase workflow: while ULV-EBL excels at pattern writing (operating approximately 10 000 times faster than c-AFM), the conventional approach to pattern erasure requires removing the

sample from the ULV-EBL chamber and using c-AFM, which is prohibitively slow. This workflow bottleneck, that ultrafast writing followed by extremely slow erasure, significantly limits the practical advantages of ULV-EBL's superior writing speed. Additionally, vacuum operation introduces another challenge: hydrocarbon contaminants in the chamber (at 10^{-6} mbar) can be deposited on the sample surface by the electron beam,^[31,32] introducing unwanted electron scattering. To address both the erasure speed limitation and surface contamination issues, we have integrated oxygen plasma capability into our ULV-EBL chamber using a plasma decontaminator (Evactron E50, Figure 5a).

Oxygen plasma is known to make LAO/STO interfaces more insulating, although the exact mechanism is not well understood. There are several possible reactions involved in the process, such as surface chemical reactions with water molecules, electron trapping induced by the oxygen plasma at the LAO surface,^[33] and the very slight removal of the top LAO layer. This treatment is rapid and affects the entire sample simultaneously. By utilizing the electrical feedthrough added to the ULV-EBL chamber, we monitored the sample conductance in situ while applying the oxygen plasma.

Our experimental sequence began with ULV-EBL patterning of an initially insulating LAO/STO sample, which increased the conductance to approximately 40 μ S (Figure 5b, green arrow). Contrary to our expectations, the subsequent oxygen plasma treatment further increased the conductivity rather than

suppressing it, with conductance rising to over 100 μS (Figure 5b, purple arrow). This unexpected behavior suggests a more complex underlying mechanism than previously understood. The discrepancy between our observations and the established understanding that oxygen plasma renders LAO/STO interfaces insulating indicates that an additional process—specifically, atmospheric exposure—plays a critical role in the conductivity modulation. Following oxygen plasma treatment in vacuum, we observed a time-dependent conductance evolution characterized by three distinct regimes: (1) an exponential-like decay that gradually diminishes while maintained in vacuum (Figure 5c,d; green region); (2) a near-linear decay during nitrogen venting (Figure 5c,d; yellow region); and (3) a rapid decrease to zero conductance within tens of seconds upon exposure to ambient air (Figure 5c,d; blue region). This sequence ultimately transforms the sample into a globally insulating state. These findings demonstrate that a combination of oxygen plasma treatment followed by controlled atmospheric exposure provides a reliable methodology for global conductivity erasure at the LAO/STO interface.

The unexpected conductance evolution during oxygen plasma treatment likely stems from multiple surface-level processes. The initial conductance spike can be attributed to plasma-generated positive ions accumulating at the LAO surface, creating a strong local electric field that electrostatically gates the underlying 2DEG. Simultaneously, plasma sputtering may generate oxygen vacancies, introducing additional charge carriers. The subsequent conductance decay occurs through distinct phases: in vacuum, surface charges gradually dissipate; during nitrogen venting, the dissipation accelerates as the gas neutralizes surface ionization; and upon air exposure, atmospheric oxygen and moisture rapidly reoxidize the LAO surface, eliminating vacancy-induced carriers and restoring the interface to its insulating state. This sequence demonstrates the LAO/STO interface's acute sensitivity to surface boundary conditions and provides insight into the chemical mechanisms underlying the erasure process.

The oxygen plasma method presents a valuable extension of the patterning toolkit: it enables rapid, in situ erasure within the SEM chamber and is highly effective for large-scale, high-throughput applications. While it does not replace local erasure with an AFM tip, it complements it by expanding the operational flexibility of the system.

3. Discussion

Compared with the previously established c-AFM approach,^[9,10,13,14,17,34] ULV-EBL achieves comparable device quality while offering distinct benefits. As shown in the direct comparison table (Table 1), c-AFM can reach a resolution of 2 nm,^[10] whereas ULV-EBL achieves 10 nm.^[18] Although ULV-EBL resolution is slightly coarser than the best c-AFM performance, both methods are still well beyond the limits of conventional fabrication methods such as electron beam lithography. Importantly, ULV-EBL offers a significant advantage in throughput, achieving up to 10 000 times faster writing speed compared to c-AFM. Both techniques have been used to realize advanced functionalities at the LAO/STO interface, including ballistic transport in 1D waveguide devices.

ULV-EBL operates under vacuum, inhibiting device degradation that occurs with c-AFM's atmospheric patterning. C-AFM is a powerful yet limited method, which provides incomparably high resolution, but is not practical for complex or large-scale devices. While conventional electron-beam lithography (EBL) with metal gates enables large-area patterning, ULV-EBL offers the same device quality and reprogrammability as c-AFM while keeping the large-area, high-speed patterning of conventional electron-beam lithography. This capability is crucial for moving from proof-of-concept quantum devices to practical arrays of qubits or quantum sensors on a large scale. Each method has its strengths and is suited to different experimental needs: ULV-EBL excels in scalability and speed, while c-AFM offers finer resolution in small-scale patterning tasks.

4. Conclusion

In summary, we have demonstrated a robust and scalable method for fabricating reconfigurable electronic structures at LaAlO₃/SrTiO₃ interfaces using ULV-EBL. This technique preserves the intrinsic properties of the oxide heterostructure while offering significant advantages in terms of processing speed, working area, and operational environment compared to established c-AFM lithography methods. The mesoscopic structures created with ULV-EBL exhibit the rich electronic phenomena characteristic of LAO/STO interfaces, including 1D superconductivity in nanochannels, nonlinear transport behavior in tunnel barriers, and quantized ballistic transport in electron waveguides.

Our investigation of oxygen plasma treatment as a pattern erasure method has revealed previously unobserved surface reaction dynamics at the LAO/STO interface. The complex conductance evolution following plasma treatment characterized by an initial conductance increase followed by a multi-stage decay process dependent on environmental conditions provides valuable insights into the coupling between surface chemistry and interfacial electronic properties in complex oxide systems. This understanding opens new avenues for controlling and manipulating oxide interfaces through targeted surface modifications.

The demonstrated capabilities of ULV-EBL—significantly faster patterning speeds (10 mm s⁻¹ vs 1 $\mu\text{m s}^{-1}$), larger working areas (> (10 cm)² vs < (90 μm)²), and operation under controlled vacuum conditions—overcome key limitations of conventional techniques, enabling the reliable fabrication of more complex and extensive interface devices. This scalability, combined with the exceptional quality of the resulting structures, positions ULV-EBL as a transformative approach for oxide interface engineering with numerous potential applications.

Looking forward, this interface patterning technology provides a promising platform for developing advanced oxide-based electronics, including high-mobility field-effect devices, novel sensors, and reconfigurable circuit elements. The technique's compatibility with van der Waals overlayers^[18,20] and potentially with oxide membranes^[35] further expands opportunities for creating hybrid materials systems with engineered functionalities. Additionally, the ability to pattern high-quality superconducting structures and ballistic electron channels at scale opens pathways for future quantum information applications, including networks of superconducting quantum devices and coherent electron

waveguides for quantum transport experiments. Overall, ULV-EBL substantially advances our ability to harness the exceptional properties of complex oxide interfaces in practical technological applications while providing a versatile platform for fundamental materials research.

5. Experimental Section

LAO/STO Sample Growth: The commercial STO (001) substrate used was 1 mm in thickness and $5 \times 5 \text{ mm}^2$ in size with TiO_2 termination, treated by buffered hydrofluoric acid for 60 s. The substrate was then annealed at $1000 \text{ }^\circ\text{C}$ under an oxygen flow of 30 sccm for 6 h prior to LAO growth. This temperature was monitored using the tube furnaces built-in temperature readout. A layer of 3.4 u.c. LAO was then grown on the STO substrate using pulsed laser deposition (PLD), under a temperature of $550 \text{ }^\circ\text{C}$ and an oxygen pressure of 10^{-3} mbar. An in situ reflection high-energy electron diffraction (RHEED) is used to monitor the thickness of deposited LAO. The sample was then post-annealed to room temperature in 1 atm oxygen. Both the growth temperature and post-growth cooldown profile were measured using a thermocouple located at the sample stage inside the PLD chamber.

Photolithography: A two-layer photolithography process was carried out with the LAO/STO sample to create both the interfacial electrodes and the top electrodes. The LAO/STO sample was spun with AZ4110 photoresist and exposed with a laser of wavelength 365 nm (120 mJ) using the Heidelberg MLA100 direct write lithography system. After developing the resist, the sample was then subjected to argon ion milling for 25 min in a chamber with 1.2×10^{-4} mbar pressure, 500 V acceleration voltage, 10 mA beam current, and an argon flow rate of 20 sccm. This achieved an etch rate of around 1 nm/min, resulting in a 25 nm deep etch that removes both the LAO layer and the top portion of STO, thereby exposing the LAO/STO interface. 3.3 nm Ti and 20.7 nm Au were deposited onto the sample following an acetone liftoff procedure. Thus, the “canvas”-like area was formed by the inter-facial electrodes. The specially designed ULV-EBL markers were also deposited within this first layer. For the second layer as surface electrodes, without ion-milling, a 4 nm Ti and 50 nm Au were deposited onto the sample connecting with the first layer interfacial electrodes and forming the bonding pads. The ion milling and metal deposition processes were implemented with Plassys Electron Beam Evaporation System MEB550S. Illustrations can be found in Supporting Information Figure S2.

ULV-EBL: As the key and the most critical step, ULV-EBL requires a scanning electron microscope (SEM) capable of low-voltage operation. A Zeiss Gemini 450 SEM was used that is integrated with a Raith electron beam lithography (EBL) pattern generator. The system was configured with electrical feedthroughs allowing in situ electrical measurements in the EBL chamber during e-beam exposure. A 100 V acceleration voltage V_{acc} was used to accelerate the electrons is consistent with avoiding the damage to the oxide structures. The working distance was kept small ($WD = 3 \text{ mm}$) in order to compensate the ultra-low V_{acc} . An in-lens secondary electron detector allows detection of the weak secondary electron signal above the sample within the small WD . The single $30 \text{ }\mu\text{m}$ aperture gives $I_b \sim 25 \text{ nA}$ beam current. The three-point alignment (TPA) and write-field alignment (WFA) was carried out at EBL markers at the edge of the sample far away from the “canvases.” Care was taken to avoid unattended exposure to the canvas region. Finally, the beam was blanked and shuttled to the canvas to expose the designed pattern as nanowires.

When working with an insulating sample such as LAO/STO, electron beam irradiation can induce significant surface charging, which in turn may distort the patterned features. To address this, several procedures are developed and implemented that effectively minimize charging during ULV-EBL exposure: 1) Grounding via Wirebonding and Electrical Feedthroughs: The sample is wirebonded and connected through in situ electrical feedthroughs during exposure. This setup enables real-time transport measurements and also ensures that the device remains electrically grounded, allowing accumulated charge to dissipate efficiently. 2)

Low Beam Current and Dose Optimization: We operate the SEM under ultra-low-voltage conditions (100–200 V), with a beam current of around 20 pA and an area dose of 30–100 $\mu\text{C}/\text{cm}^2$. These parameters are significantly lower than those used in standard resist-based EBL processes and are optimized for LAO/STO to minimize charging while ensuring successful patterning. 3) Avoiding Precharging of the Device Area: To prevent unintended precharging of the “canvas” region, all alignment and beam adjustments were performed in areas far from the device. The beam remains blanked while moving to the canvas, and exposure occurs only during the intended patterning step. After implementing these procedures, AFM imaging of the exposed regions was performed and found no discernible distortion in the patterns when compared with the original design layout (see Supporting Information Figure S1).

Dilution Refrigerator: The sample was cooled down in a Quantum Design Physical Property Measurement System (PPMS) with a dilution refrigerator insert which can go from $T = 300 \text{ K}$ to $T = 50 \text{ mK}$. A Krohn-Hite Model 7008 amplifier and set of National Instruments PXI-4461 DAQ cards were used to perform electrical transport measurements.

Supporting Information

Supporting Information is available from the Wiley Online Library or from the author.

Acknowledgements

The authors acknowledge financial support for this research from NSF DMR-2225888 (J.L.), Gordon and Betty Moore Foundation’s EPIQS Initiative, Grant 284, GBMF9065 (C.B.E.), and a Vannevar Bush Faculty Fellowship N00014-20-1-2844 (C.B.E). Transport measurement at the University of Wisconsin–Madison was supported by the US Department of Energy (DOE), Office of Science, Office of Basic Energy Sciences (BES), under award number DE-FG02-06ER46327. D.Y. acknowledges the discussion with Jiangfeng Yang.

Conflict of Interest

The authors have no conflicts to disclose.

Data Availability Statement

The data that support the findings of this study are available from the corresponding author upon reasonable request.

Keywords

complex oxide, electron beam lithography, nanowires, strontium titanate, superconductivity

Received: May 16, 2025
Revised: August 19, 2025
Published online: September 4, 2025

- [1] Y.-Y. Pai, A. Tylan-Tyler, P. Irvin, J. Levy, *Rep. Prog. Phys.* **2018**, *81*, 036503.
- [2] A. Ohtomo, H. Y. Hwang, *Nature* **2004**, *427*, 423.
- [3] S. Thiel, G. Hammerl, A. Schmehl, C. W. Schneider, J. Mannhart, *Science* **2006**, *313*, 1942.

- [4] J. F. Schooley, W. R. Hosler, M. L. Cohen, *Phys. Rev. Lett.* **1964**, *12*, 474.
- [5] C. S. Koonce, M. L. Cohen, J. F. Schooley, W. R. Hosler, E. R. Pfeiffer, *Phys. Rev.* **1967**, *163*, 380.
- [6] A. Brinkman, M. Huijben, M. Van Zalk, J. Huijben, U. Zeitler, J. C. Maan, W. G. Van der Wiel, G. Rijnders, D. H. A. Blank, H. Hilgenkamp, *Nat. Mater.* **2007**, *6*, 493.
- [7] A. D. Caviglia, M. Gabay, S. Gariglio, N. Reyren, C. Cancellieri, J. M. Triscone, *Phys. Rev. Lett.* **2010**, *104*, 126803.
- [8] M. Ben Shalom, A. Ron, A. Palevski, Y. Dagan, *Phys. Rev. Lett.* **2010**, *105*, 206401.
- [9] C. Cen, S. Thiel, G. Hammerl, C. W. Schneider, K. E. Andersen, C. S. Hellberg, J. Mannhart, J. Levy, *Nat. Mater.* **2008**, *7*, 298.
- [10] C. Cen, S. Thiel, J. Mannhart, J. Levy, *Science* **2009**, *323*, 1026.
- [11] G. Cheng, P. F. Siles, F. Bi, C. Cen, D. F. Bogorin, C. W. Bark, C. M. Folkman, J.-W. Park, C.-B. Eom, G. Medeiros-Ribeiro, J. Levy, *Nat. Nanotechnol.* **2011**, *6*, 343.
- [12] G. Cheng, M. Tomczyk, S. Lu, J. P. Veazey, M. Huang, P. Irvin, S. Ryu, H. Lee, C.-B. Eom, C. S. Hellberg, J. Levy, *Phys. Rev. Lett.* **2011**, *106*, 196.
- [13] A. Annadi, G. Cheng, H. Lee, J.-W. Lee, S. Lu, A. Tylan-Tyler, M. Briggeman, M. Tomczyk, M. Huang, D. Pekker, C.-B. Eom, P. Irvin, J. Levy, *Nano Lett.* **2018**, *18*, 4473.
- [14] M. Briggeman, H. Lee, J.-W. Lee, K. Eom, F. Damanet, E. Mansfield, J. Li, M. Huang, A. J. Daley, C.-B. Eom, P. Irvin, J. Levy, *Nat. Phys.* **2021**, *17*, 782.
- [15] Y.-Y. Pai, H. Lee, J.-W. Lee, A. Annadi, G. Cheng, S. Lu, M. Tomczyk, M. Huang, C.-B. Eom, P. Irvin, J. Levy, *Phys. Rev. Lett.* **2018**, *120*, 147001.
- [16] G. Cheng, M. Tomczyk, S. Lu, J. P. Veazey, M. Huang, P. Irvin, S. Ryu, H. Lee, C. B. Eom, C. S. Hellberg, J. Levy, *Nature* **2015**, *521*, 196.
- [17] M. Briggeman, M. Tomczyk, B. Tian, H. Lee, J.-W. Lee, Y. He, A. Tylan-Tyler, M. Huang, C.-B. Eom, D. Pekker, R. S. K. Mong, P. Irvin, J. Levy, *Science* **2020**, *367*, 769.
- [18] D. Yang, S. Hao, J. Chen, Q. Guo, M. Yu, Y. Hu, K. Eom, J.-W. Lee, C.-B. Eom, P. Irvin, J. Levy, *Appl. Phys. Lett.* **2020**, *117*, 253103.
- [19] M. Yu, C. Liu, D. Yang, X. Yan, Q. Du, D. D. Fong, A. Bhattacharya, P. Irvin, J. Levy, *Nano Lett.* **2022**, *22*, 6062.
- [20] D. Yang, Q. Cao, E. Akyuz, J. Hayden, J. Nordlander, I. Mercer, M. Yu, R. Ramachandran, P. Irvin, J.-P. Maria, B. M. Hunt, J. Levy, *Nano Lett.* **2024**, *24*, 16231.
- [21] A. Ron, E. Maniv, D. Graf, J.-H. Park, Y. Dagan, *Phys. Rev. Lett.* **2014**, *113*, 216801.
- [22] M. Tinkham, in *Introduction to Superconductivity*, Courier Corporation.
- [23] A. Bezryadin, C. N. Lau, M. Tinkham, *Nature* **2000**, *404*, 971.
- [24] C. N. Lau, N. Markovic, M. Bockrath, A. Bezryadin, M. Tinkham, *Phys. Rev. Lett.* **2001**, *87*, 217003.
- [25] M. Z. Minhas, A. M \ddot{u} ller, F. Heyroth, H. H. Blaschek, G. Schmidt, *Sci. Rep.* **2017**, *7*, 5215.
- [26] L. Chen, E. Sutton, H. Lee, J.-W. Lee, J. Li, C.-B. Eom, P. Irvin, J. Levy, *Light: Sci. Appl.* **2019**, *8*, 24.
- [27] R. Landauer, *IBM J. Res. Develop.* **1957**, *1*, 223.
- [28] D. C. Langreth, E. Abrahams, *Phys. Rev. B* **1981**, *24*, 2978.
- [29] M. Briggeman, J. Li, M. Huang, H. Lee, J.-W. Lee, K. Eom, C.-B. Eom, P. Irvin, J. Levy, *Sci. Adv.* **2020**, *6*, eaba6337.
- [30] R. Ramachandran, S. Anand, K. Eom, K. Lee, D. Yang, M. Yu, S. Biswas, A. Nethwewala, C.-B. Eom, E. Carlson, P. Irvin, J. Levy, *arXiv* **2025**.
- [31] O. Guise, H. Marbach, J. Levy, J. Ahner, J. T. Yates, *Surf. Sci.* **2004**, *571*, 128.
- [32] C. W. Petz, D. Yang, A. F. Myers, J. Levy, J. A. Floro, *Appl. Phys. Lett.* **2014**, *104*, 013108.
- [33] W. Dai, S. Adhikari, A. C. Garcia-Castro, A. H. Romero, H. Lee, J.-W. Lee, S. Ryu, C.-B. Eom, C. Cen, *Nano Lett.* **2016**, *16*, 2739.
- [34] M. Briggeman, J. Li, M. Huang, H. Lee, J.-W. Lee, K. Eom, C.-B. Eom, P. Irvin, J. Levy, *arXiv* **2020**, *6*, eaba6337.
- [35] K. Eom, M. Yu, J. Seo, D. Yang, H. Lee, J.-W. Lee, P. Irvin, S. H. Oh, J. Levy, C.-B. Eom, *Phys. Rev. Lett.* **2020**, *124*, 076101.